

# Measurement of the forward $\eta$ meson production rate in p-p collisions at $\sqrt{s} = 13$ TeV with the LHCf-Arm2 detector

O. Adriani,<sup>a,b</sup> E. Berti,<sup>a</sup> P. Betti,<sup>a,b</sup> L. Bonechi,<sup>a</sup> M. Bongi,<sup>a,b</sup> R. D'Alessandro,<sup>a,b</sup> S. Detti,<sup>a</sup> M. Hagenauer,<sup>c</sup> Y. Itow,<sup>d,e</sup> K. Kasahara,<sup>f</sup> Y. Kitagami,<sup>d</sup> M. Kondo,<sup>d</sup> Y. Matsubara,<sup>d,1</sup> H. Menjo,<sup>d</sup> Y. Muraki,<sup>d</sup> K. Ohashi,<sup>d</sup> P. Papini,<sup>a</sup> G. Piparo,<sup>g,h,i,2</sup> S. Ricciarini,<sup>a,j</sup> T. Sako,<sup>k</sup> N. Sakurai,<sup>l,3</sup> M. Scaringella,<sup>a</sup> Y. Shimizu,<sup>m</sup> T. Tamura,<sup>m</sup> A. Tiberio,<sup>a,b</sup> S. Torii,<sup>n</sup> A. Tricomi,<sup>g,h,i</sup> W.C. Turner<sup>o</sup> and K. Yoshida<sup>f</sup>

<sup>a</sup>INFN, Section of Firenze,

Via G. Sansone 1, Sesto Fiorentino I-50019, Italy

<sup>b</sup>Department of Physics and Astronomy, University of Firenze,

Via G. Sansone 1, Sesto Fiorentino I-50019, Italy

<sup>c</sup>Ecole-Polytechnique, Route de Saclay, Palaiseau 91128 CEDEX, France

<sup>d</sup>Institute for Space-Earth Environmental Research, Nagoya University,

Furocho, Chikusaku, Nagoya, Aichi 464-8602, Japan

<sup>e</sup>Kobayashi-Maskawa Institute for the Origin of Particles and the Universe, Nagoya University,

Furocho, Chikusaku, Nagoya, Aichi 464-8602, Japan

<sup>f</sup>Faculty of System Engineering, Shibaura Institute of Technology,

307 Fukusaku, Minuma-ku, Saitama 337-8570, Japan

<sup>g</sup>INFN, Section of Catania,

Via Santa Sofia 64, Catania 95123, Italy

<sup>h</sup>Department of Physics and Astronomy "Ettore Majorana", University of Catania,

Via Santa Sofia 64, Catania 95123, Italy

<sup>i</sup>Centro Siciliano di Fisica Nucleare e Struttura della Materia (CSFNMSM),

Via Santa Sofia 64, Catania 95123, Italy

<sup>j</sup>Istituto di Fisica Applicata "Nello Carrara" (IFAC-CNR),

Via Madonna Del Piano 10, Sesto Fiorentino I-50019, Italy

<sup>k</sup>Institute for Cosmic Ray Research (ICRR), University of Tokyo,

5-1-5 Kashiwanoha, Kashiwa, Chiba 277-8582, Japan

<sup>l</sup>Tokushima University, Tokushima 770-8051, Japan

<sup>1</sup>Now at Center for Muon Science and Technology, Chubu University, 1200 Matsumoto, Kasugai, Aichi 487-8601, Japan.

<sup>2</sup>Corresponding author.

<sup>3</sup>Now at Faculty of Design Technology, Osaka Sangyo University, 3-1-1 Nakagauchi, Daito City, Osaka 574-8530, Japan.

<sup>m</sup>*Department of Applied Physics, Kanagawa University,  
Yokohama, Kanagawa 221-8686, Japan*

<sup>n</sup>*Waseda Research Institute for Science and Engineering (RISE), Waseda University,  
17 Kikuicho, Shinjuku, Tokyo 162-0044, Japan*

<sup>o</sup>*Lawrence Berkeley National Laboratory (LBNL),  
1 Cyclotron Rd, Berkeley, CA 94720, U.S.A.*

*E-mail:* [adriani@fi.infn.it](mailto:adriani@fi.infn.it), [eugenio.berti@fi.infn.it](mailto:eugenio.berti@fi.infn.it),  
[betti@fi.infn.it](mailto:betti@fi.infn.it), [lorenzo.bonechi@fi.infn.it](mailto:lorenzo.bonechi@fi.infn.it),  
[massimo.bongi@fi.infn.it](mailto:massimo.bongi@fi.infn.it), [candi@fi.infn.it](mailto:candi@fi.infn.it),  
[sebastiano.detti@fi.infn.it](mailto:sebastiano.detti@fi.infn.it), [Maurice.Haguenauer@cern.ch](mailto:Maurice.Haguenauer@cern.ch),  
[itow@isee.nagoya-u.ac.jp](mailto:itow@isee.nagoya-u.ac.jp), [kasahara@icrr.u-tokyo.ac.jp](mailto:kasahara@icrr.u-tokyo.ac.jp),  
[kitagami.yuga@isee.nagoya-u.ac.jp](mailto:kitagami.yuga@isee.nagoya-u.ac.jp), [kondo.moe@i.mbox.nagoya-u.ac.jp](mailto:kondo.moe@i.mbox.nagoya-u.ac.jp),  
[ymatsu@isee.nagoya-u.ac.jp](mailto:ymatsu@isee.nagoya-u.ac.jp), [menjo@isee.nagoya-u.ac.jp](mailto:menjo@isee.nagoya-u.ac.jp),  
[muraki@isee.nagoya-u.ac.jp](mailto:muraki@isee.nagoya-u.ac.jp), [ohashi.ken@isee.nagoya-u.ac.jp](mailto:ohashi.ken@isee.nagoya-u.ac.jp),  
[papini@fi.infn.it](mailto:papini@fi.infn.it), [giuseppe.piparo@ct.infn.it](mailto:giuseppe.piparo@ct.infn.it) ,  
[ricciarini@fi.infn.it](mailto:ricciarini@fi.infn.it), [sako@isee.nagoya-u.ac.jp](mailto:sako@isee.nagoya-u.ac.jp),  
[nsakurai@icrr.u-tokyo.ac.jp](mailto:nsakurai@icrr.u-tokyo.ac.jp), [scaringella@fi.infn.it](mailto:scaringella@fi.infn.it),  
[yshimizu@kanagawa-u.ac.jp](mailto:yshimizu@kanagawa-u.ac.jp), [ttamura@kanagawa-u.ac.jp](mailto:ttamura@kanagawa-u.ac.jp),  
[alessio.tiberio@fi.infn.it](mailto:alessio.tiberio@fi.infn.it), [torii.shoji@waseda.jp](mailto:torii.shoji@waseda.jp),  
[alessia.tricomi@ct.infn.it](mailto:alessia.tricomi@ct.infn.it), [WCTurner@lbl.gov](mailto:WCTurner@lbl.gov),  
[yoshida@sic.shibaura-it.ac.jp](mailto:yoshida@sic.shibaura-it.ac.jp)

ABSTRACT: The forward  $\eta$  mesons production has been observed by the Large Hadron Collider forward (LHCf) experiment in proton-proton collision at  $\sqrt{s} = 13$  TeV. This paper presents the measurement of the inclusive production rate of  $\eta$  in  $p_T < 1.1$  GeV/c, expressed as a function of the Feynman- $x$  variable. These results are compared with the predictions of several hadronic interaction models commonly used for the modelling of the air showers produced by ultra-high energy cosmic rays. This is both the first measurement of  $\eta$  mesons from LHCf and the first time a particle containing strange quarks has been observed in the forward region for high-energy collisions. These results will provide a powerful constraint on hadronic interaction models for the purpose of improving the understanding of the processes underlying the air showers produced in the Earth's atmosphere by ultra-energetic cosmic rays.

KEYWORDS: Forward Physics, Hadron-Hadron Scattering, Particle and Resonance Production, QCD

ARXIV EPRINT: [2305.06633](https://arxiv.org/abs/2305.06633)

---

## Contents

<b>1</b>	<b>Introduction</b>	<b>1</b>
<b>2</b>	<b>The LHCf experiment</b>	<b>2</b>
<b>3</b>	<b>Summary of data taking conditions and Monte Carlo simulations methodology</b>	<b>3</b>
3.1	Data taking conditions	3
3.2	Monte Carlo simulations	4
<b>4</b>	<b>Analysis framework</b>	<b>5</b>
4.1	$\eta$ event reconstruction and selection	5
4.1.1	Hit position reconstruction	6
4.1.2	Energy reconstruction	6
4.1.3	Single photon identification	6
4.1.4	$\eta$ reconstruction and background subtraction	7
4.2	Corrections	8
4.2.1	Selection correction	8
4.2.2	Acceptance and branching ratio correction	9
4.2.3	Multi-hit correction	10
4.3	Systematic uncertainties	12
4.3.1	Energy scale	12
4.3.2	PID	13
4.3.3	Beam-center stability	13
4.3.4	Luminosity	13
4.3.5	Background subtraction	13
4.3.6	MC related correction	14
<b>5</b>	<b>Results</b>	<b>14</b>
<b>6</b>	<b>Conclusions</b>	<b>14</b>
<b>A</b>	<b>Production rate distributions at the detector level</b>	<b>16</b>
<b>B</b>	<b>Cross section tables</b>	<b>17</b>

---

## 1 Introduction

Due to the steeply decreasing flux, ultra-high energy cosmic rays (UHECRs) can be measured only indirectly by observing the air showers induced in the Earth's atmosphere. Many ground-based experiments performed measurements of flux, composition and anisotropy of UHECRs [1–7]. Recently the Pierre Auger Observatory (PAO [8]) and Telescope Array (TA [9]) experiments made the most precise measurements using hybrid detection techniques. The information about the primary cosmic rays is obtained by inferring the air

shower characteristics from an array of surface detectors to observe charged particles at ground and a stereoscopic system of fluorescence detectors to observe light emission due to the excitation and de-excitation of molecules in the atmosphere. Despite the progress made through combining these techniques, the interpretation of the results obtained on mass composition still needs to be clarified [10–12]. This is because critical parts of the data analyses depend on the simulation of the air showers. The hadronic interaction models used to predict the consecutive elementary interactions during the shower development are a fundamental input in the simulations. Models must provide predictions on both “hard” and “soft” processes. While the Standard Model properly describes hard processes, soft processes need phenomenological treatment because of the low transferred four-momentum, which forbids the development of a perturbation theory because of the high values of the QCD coupling constant. Soft processes can be described using Gribov-Regge theories [13, 14], which involve the exchange of virtual quasi-particles called “Pomerons” in the interactions. Since there are different ways to implement Gribov-Regge theories, various models based on different implementations provide conflicting results on particle production. In order to reduce the differences between models, it is necessary to have high-energy calibration data. The Large Hadron Collider (LHC [15]) is the most suitable place to perform these measurements since a proton-proton collision at  $\sqrt{s} = 13$  TeV is equivalent to the interaction of about  $10^{17}$  eV cosmic ray with a proton at rest. Indeed, many experiments have provided calibration data for hadronic interaction models in recent years (see [16] for a review of the most up-to-date results). Among these, the Large Hadron Collider forward (LHCf [17]) experiment was designed to measure the production of neutral particles at very high pseudorapidities, which is one of the fundamental parameters of the models, since soft processes are mainly associated with the forward particle production. This paper reports the first LHCf measurement of  $\eta$  meson inclusive production rate, which was accomplished using the LHCf-Arm2 detector. The importance of this observation relies on the fact that  $\eta$  meson is a probe for the contribution of strange quarks to the hadronization mechanism. Differences in this parameter induce a large discrepancy in the expected  $\eta$  production cross section among the models [18]. In addition, the photons produced in the  $\eta$  decays are the second dominant photon sources in high-energy hadronic interactions after  $\pi^0$  production and are relevant for the development of air showers. This paper is organized as follows. Section 2 describes the LHCf experimental apparatus. In section 3, we summarize the experimental dataset and the Monte Carlo (MC) simulation methodology. Section 4 explains the general analysis strategy, including the reconstruction procedure, the selection criteria, the calculation of corrections for the final spectrum and the effects contributing to the systematic uncertainty. In section 5, the analysis results are presented and compared with the predictions of several hadronic interaction models. Finally, the paper conclusions can be found in section 6.

## 2 The LHCf experiment

The LHCf detectors are two independent sampling and imaging calorimeters, called Arm1 and Arm2. Each calorimeter is composed of two towers, made of tungsten absorbers

alternated with 16 GSO scintillator layers. The lateral profile of the shower is reconstructed by imaging layers inserted at different depths. Arm1 uses four pairs of X–Y GSO bar-bundle hodoscopes [19], while Arm2 uses four pairs of X–Y silicon microstrip detectors, in the first two pairs the X and Y layers are placed in contact, while in the last two pairs they are detached at different depths [20]. The total length of the two arms is about 21 cm, equivalent to 44 radiation lengths or 1.6 interaction lengths. The calorimeter towers have transversal dimensions of  $20\text{ mm} \times 20\text{ mm}$  and  $40\text{ mm} \times 40\text{ mm}$  for Arm1,  $25\text{ mm} \times 25\text{ mm}$  and  $32\text{ mm} \times 32\text{ mm}$  for Arm2. This configuration allows an optimal reconstruction of  $\pi^0$  and  $\eta$  mesons from the simultaneous detection of the two photons generated by their decay. The detectors are located in two regions on opposite sides of LHC Interaction Point 1 (IP1), at a distance of 141.05 m from IP1. In these regions, called Target Neutral Absorbers (TAN), the beam vacuum chamber makes a Y-shaped transition from a single beam tube facing the IP1 to two separate beam tubes joining the arcs of LHC. In this position the LHCf experiment accesses to the measurement of the high-energy neutral particle flux produced by hadronic collisions with a pseudorapidity  $|\eta| > 8.4$  while charged particles directed toward the LHCf detector positions are wiped out by the D1 dipole magnet. The performances of the detector were evaluated during beam tests at the CERN Super Proton Synchrotron (SPS) [21, 22]. Concerning the reconstruction of photons, the estimated energy and position resolution values of the LHCf-Arm2 detector are better than 3% and  $40\text{ }\mu\text{m}$ , respectively, for photons with energy above 200 GeV [21]. More details on the scientific goals and the performance of the LHCf experiment are discussed in previous reports [21–23]. For this analysis, we used only the LHCf-Arm2. A schematic representation of this detector is illustrated in figure 1.

### 3 Summary of data taking conditions and Monte Carlo simulations methodology

#### 3.1 Data taking conditions

The two experimental datasets used for this analysis were acquired by a special LHCf run on June 12th–13th, 2015, corresponding to LHC Fill 3855. During this dedicated low luminosity fill, 29 bunches collided at IP1 with a half crossing angle of  $145\text{ }\mu\text{rad}$  and a  $\beta^*$  of 19 m. Other 6 and 2 non-colliding bunches circulated in the clockwise and counter-clockwise beams, respectively, which were used to estimate the background due to interactions between the produced particles and the residual gas molecules in the beam pipe. The first dataset was taken from 22:32 to 1:30 (CEST), with an instantaneous luminosity of  $L = (3 - 5) \times 10^{28}\text{ cm}^{-2}\text{ s}^{-1}$  (as measured by the ATLAS experiment [24]) and an average number of collisions per bunch crossing  $\mu$  in the range of [0.007, 0.012]. The second dataset was taken from 1:40 to 12:10 (CEST), with an instantaneous luminosity of  $L = (13 - 17) \times 10^{28}\text{ cm}^{-2}\text{ s}^{-1}$  [24] and an average number of collisions per bunch crossing  $\mu$  in the range of [0.03, 0.04]. Considering the LHCf data acquisition live time, the integrated luminosities were estimated to be  $0.194\text{ nb}^{-1}$  and  $1.938\text{ nb}^{-1}$  for the first and the second dataset, respectively. Both datasets were used in this analysis for a total of 8.4 million triggered events.

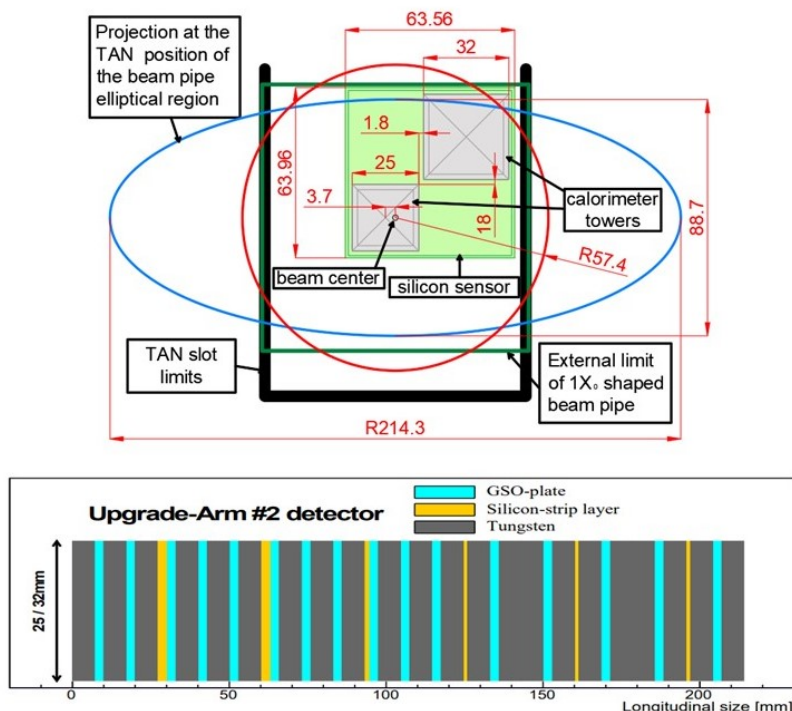


**Figure 1.** Schematic view of the LHCf-Arm2 detector. The transversal view of the detector inside the TAN slot is illustrated in the top panel, while the bottom panel shows the longitudinal structure, including the sizes and the arrangement of the layers.

### 3.2 Monte Carlo simulations

Monte Carlo (MC) simulations were used in this work to perform several analysis tasks. The full MC simulations with the same configuration of the LHCf consist of three steps: (1) hadronic interaction of proton-proton collisions at  $\sqrt{s} = 13$  TeV at IP1, (2) transport of produced particles from IP1 to LHCf-Arm2 location and (3) interactions with the detector. The three parts of the simulation were performed using simulation packages Cosmos 7.633 [25] and EPICS 9.15 [26]. The full simulation has been performed starting from the events generated by two hadronic interaction models, QGSJET II-04 [27] and EPOS-LHC [28]. The interaction of the collision products with the detector was simulated using DPMJET 3.04 [29]. As described in sections 4.2–4.3, the two full simulation datasets were used to calculate some correction factors and systematic uncertainties. The full QGSJET II-04 simulation was also used to compute the energy-dependent cut function for particle identification. To compare our results with hadronic interaction model predictions, we used the CRMC package [30], which acts as a frontend for the models under consideration. In this way, we generated a large simulation dataset for the models that are commonly used for air shower simulations: QGSJET II-04, EPOS-LHC, SIBYLL 2.3 [31] and DPMJET 3.06. In all the four cases, we considered the particles directly produced in the collisions or by the decay of unstable particles with  $c \cdot \tau < 1$  cm. The number of events and the inelastic cross section of each model is listed in table 1. More details about the simulation’s methodology can be found in [32].

Model	QGSJET	EPOS	SIBYLL	DPMJET
$\sigma_{\text{inel}}$ [mb]	80.17	78.98	79.86	80.14
$N_{\text{ev}}$	$9.96 \cdot 10^7$	$9.90 \cdot 10^7$	$10^8$	$10^8$

**Table 1.** Total inelastic cross section  $\sigma_{\text{inel}}$  for p-p collisions at  $\sqrt{s} = 13$  TeV and the number of events ( $N_{\text{ev}}$ ) for each hadronic interaction model used for the comparison with experimental data (version number is omitted).

## 4 Analysis framework

### 4.1 $\eta$ event reconstruction and selection

The LHCf-Arm2 detector can identify  $\eta$  mesons by reconstructing the two photons produced in the decay  $\eta \rightarrow \gamma\gamma$ , which occurs with a branching ratio of  $(39.41 \pm 0.18)\%$  [33]. The two photons can enter one in each detector tower (Type I events, left panel of figure 2) or both in the same tower (Type II events, right panel of figure 2). The reconstruction and selection algorithms for  $\eta$  mesons are similar to that developed for Type I  $\pi^0$  analysis [32, 34]. Type II  $\eta$  studies however cannot be carried out in this analysis since the acceptance for this type of event in the LHCf-Arm2 detector is very small. The energy threshold for Type II  $\eta$  events is given by  $E_{\text{min}} = 2M_\eta L/d_{\text{max}}$ , where  $M_\eta$  is the mass of the  $\eta$ ,  $L$  is the distance between IP1 and the LHCf detector, about 141.05 m, and  $d_{\text{max}}$  is the maximum distance between the impact positions of the two photons. Considering the maximum distance between photon hit positions for Type II events, which correspond to the diagonal of the large tower of LHCf-Arm2,  $d_{\text{max}} = 39.6$  mm, it turns out that only Type II  $\eta$  with energy threshold  $E_{\text{min}} \approx 3900$  GeV can be detected by the LHCf-Arm2 detector. We do not have enough events of this type in the datasets to obtain a significant result for Type II, hence we limit our analysis to Type I events. The  $\eta$  mesons produced in the collisions decay very close to the interaction point IP1. Indeed we calculate the opening angle  $\theta$  from the transverse distance between photon impact points at the LHCf-Arm2 detector assuming that the decay happened at the IP1 (about 141.05 m from the detector). As a consequence, the opening angle is very small and constrained by  $\theta \leq 0.6$  mrad. We also reconstructed the kinematic variables of  $\eta$  (energy,  $p_T$  and  $p_z$ ) by using the energies and positions of the photons hitting the calorimeter. The minimum distance between photon hit positions is given by  $d_{\text{min}} = 2M_\eta L/E_{\text{max}}$ , with  $E_{\text{max}} = 6500$  GeV, and it is equal to  $d_{\text{min}} = 23.85$  mm. Since this value is much larger than the LHCf-Arm2 position resolution for electromagnetic showers with energy above 200 GeV (about 40  $\mu\text{m}$ , as seen in section 2), there is not  $\eta$  loss due to indistinguishable photons pairs. The  $\eta$  inclusive production rate has been expressed in terms of the Feynman- $x$  variable, which was calculated as  $x_F = 2p_z/\sqrt{s}$ . Despite interesting information about scaling laws can be extracted by looking at the  $\eta$  meson  $x_F$  distribution in several transverse momentum  $p_T$  bins, due to the limited statistics we were able to extract such distribution for only one bin, with  $0.0 \text{ GeV}/c \leq p_t < 1.1 \text{ GeV}/c$ . The data analysis algorithm consists of five steps: hit position reconstruction, energy reconstruction, single photon identification,  $\eta$  reconstruction and background subtraction.

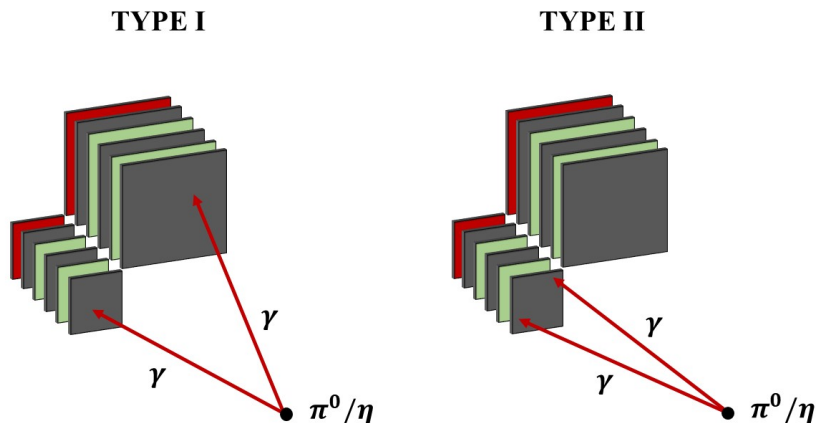


**Figure 2.** Schematic representation of a  $\pi^0$  or  $\eta$  decay observed by the LHCf-Arm2 detector. Photons can enter in two different towers (Type I event, left panel) or both in the same tower (Type II event, right panel). The LHCf-Arm2 representation is not on scale.

#### 4.1.1 Hit position reconstruction

The transverse position of particles hitting the LHCf-Arm2 detector is determined using the lateral profile distribution recorded by the silicon microstrip position-sensitive layers. Using an algorithm based on the TSppectrum class [35] of the ROOT analysis framework [36], it is possible to separate events with a single particle hitting the tower (single-hit events) from that with more than one particle in the same tower (multi-hit events). Single-hit events present only one peak in the lateral profile distribution, while several peaks are identified for multi-hit events. Multi-hit events are rejected from the analysis. The loss of  $\eta$  events due to the multi-hit cut is corrected, as explained in section 4.2.3. The lateral distributions are fit to superimposed Lorentzian functions (one for each peak) to precisely estimate the shower peak position, height, and width. Particles with hit position within 2 mm from the edges of the two towers are excluded to avoid significant effects due to the lateral shower’s leakage.

#### 4.1.2 Energy reconstruction

The energy of photons is reconstructed from the deposited energy in the calorimeter layers. Energy deposits are converted from the charge information using the conversion coefficients calculated at the SPS beam tests [21]. The deposited energy is computed using the sum of the releases from the 2nd to 13th layer and is corrected for the light yield efficiency of the scintillators and the leakage effects [17]. Then, using an empirical polynomial function, we convert the total deposited energy into the primary energy. Events with energy below 200 GeV are not considered in the analysis to reject the particles produced in the beam pipe interactions and avoid uncertainties due to the trigger inefficiency.

#### 4.1.3 Single photon identification

The particle identification (PID) algorithm used for this analysis aims to separate photons from neutral hadron background, mainly due to neutrons. We performed the selection

Event type	Type I
Number of hits	single-hit for each tower
Incident position	Within 2 mm from the edge of calorimeter
Energy threshold	$E > 200$ GeV
PID	Photonlike [ $L_{90\%} < f_{L_{90\%}}(E)$ ]

**Table 2.** List of single-photon selection criteria.

by using one particular shower feature, the longitudinal distance measured from the first calorimeter layer to the depth where the total energy deposition is 90% of the total shower energy deposition. This variable is called  $L_{90\%}$  and is expressed in units of radiation length  $[X_0]$ . In a previous study [32], we demonstrated that  $L_{90\%}$  has a strong discrimination power to distinguish between pure electromagnetic showers and the background showers produced by hadrons. PID criteria are expressed as a function of the energy of the particles hitting the calorimeter  $f_{L_{90\%}}(E)$ , in order to impose a constant selection efficiency of 90% in the whole photon energy range. The two functions, one for each tower, are calculated using the full QGSJET II-04 model simulation. To calculate the cut functions, we applied all the single-photon selection criteria used for the analysis, described in the previous sections and listed in table 2. Using the MC truth of the simulation, we considered only photon pairs produced in the  $\eta$  decays. This is necessary to maintain the selection efficiency of  $\eta$  under control in the relevant energy range for  $\eta$  detection, since most of the photons that pass the imposed criteria come from the decay of  $\pi^0$ s, which possess very different kinematics than  $\eta$  due to their mass difference. The residual hadron contamination (typically 10%) can be estimated as a function of energy using MC simulation and it is corrected together with the 90% efficiency. It is removed during the background subtraction procedure described in section 4.1.4. The selection inefficiency is corrected in section 4.2.1, while the uncertainty related to the PID is calculated in section 4.3.2.

#### 4.1.4 $\eta$ reconstruction and background subtraction

Candidates  $\eta$  mesons are selected by looking at the characteristic peak in the di-photon invariant mass spectrum around the  $\eta$  rest mass. We use the reconstructed energy and position of selected photon pairs to compute the invariant mass  $M_{\gamma\gamma}$  according to the formula:

$$M_{\gamma\gamma} = \sqrt{2E_1E_2(1 - \cos\theta)}, \tag{4.1}$$

where  $E_1$  and  $E_2$  are the energies of the two photons, and  $\theta$  is the opening angle in the laboratory reference system. The peak of the distribution occurred at  $M_{\gamma\gamma} = (533.3 \pm 1.1)$  MeV/ $c^2$ . The world averaged  $\eta$  rest mass is  $M_\eta = 547.86$  MeV/ $c^2$  [33], so a shift of  $(-2.65 \pm 0.20)\%$  is present in our data. We verified that a compatible shift was also present in the invariant mass peak associated with the decay of  $\pi^0$  into two photons hitting the two different towers of LHCf-Arm2, and we found a consistent value of  $(-2.57 \pm 0.04)\%$ . As motivated in section 4.3.1, where it is shown that the two shift values are consistent within the errors and are also compatible with the uncertainty on the absolute energy

scale, we applied an artificial shift of +2.65% to the energies of single photons to correct the peak position according to the reference value. After this correction, the  $\eta$  meson peak became concentrated around the value  $M_{\gamma\gamma} = (548.1 \pm 1.1) \text{ MeV}/c^2$ . The reported errors on invariant mass values and shifts are statistical only.

Since the  $\eta$  statistic was very low in the analysed dataset, we could not extract the  $x_F$  distribution and remove the combinatorial background using a template fit for each  $x_F$  bin. We, therefore, decided to use a sideband method [32]. First, we performed a binned fit of the distribution using a composite model made by the sum of an asymmetric Gaussian function for the signal component and a third-order Chebyshev polynomial function for the background component. The expected mean  $\langle m \rangle$  and the  $1\sigma$  deviations ( $\sigma_l$  for the left side and  $\sigma_r$  for the right side) have been used to define the signal region within  $[\langle m \rangle - 3\sigma_l, \langle m \rangle + 3\sigma_r]$  and two background regions, within  $[\langle m \rangle - 7\sigma_l, \langle m \rangle - 4\sigma_l]$  and  $[\langle m \rangle + 4\sigma_r, \langle m \rangle + 7\sigma_r]$ . The invariant mass distribution, the composite fit, the signal region and the two background regions are displayed in figure 3. The background component in the signal region was estimated by scaling the sum of the  $x_F$  distributions in the background regions for the ratio between the integrals of the Chebyshev polynomial function in the signal and background regions. Then it was subtracted to the signal region  $x_F$  distribution. Using this method we found about 1500  $\eta$  mesons in the dataset. The uncertainty of the background subtraction method was estimated using the full reconstructed QGSJET II-04 simulation, as described in section 4.3.5.

## 4.2 Corrections

The corrections applied to the  $x_F$  spectrum of  $\eta$  are discussed in this section. Each correction is described in sections 4.2.1–4.2.3. For the selection and multi-hit corrections we used two fully reconstructed MC simulations, described in section 3.2, based on the QGSJET II-04 and EPOS-LHC models. We validated the choice of the two models by comparing the detector level  $x_F$  distribution of the experimental data and the Monte Carlo simulations, as described in appendix A. Figure 4 shows distributions of correction factors as a function of  $x_F$ .

### 4.2.1 Selection correction

First, the signal distribution has to be corrected for the selection inefficiency and the smearing effects. Both effects are corrected simultaneously using the fully reconstructed simulation based on QGSJET II-04 and EPOS-LHC. For both models, we took the ratio between the  $\eta$  candidate  $x_F$  distribution, obtained using the same reconstruction algorithm as experimental data, and the true  $x_F$  distribution of  $\eta$  mesons. The final correction factor is estimated from the average of the values obtained from the two models. The correction procedure was validated by performing a closure test between the particle-level distributions and the corrected detector level distributions for both simulations. To consider the differences between the models, we add a systematic error related to this correction, described in section 4.3.6.

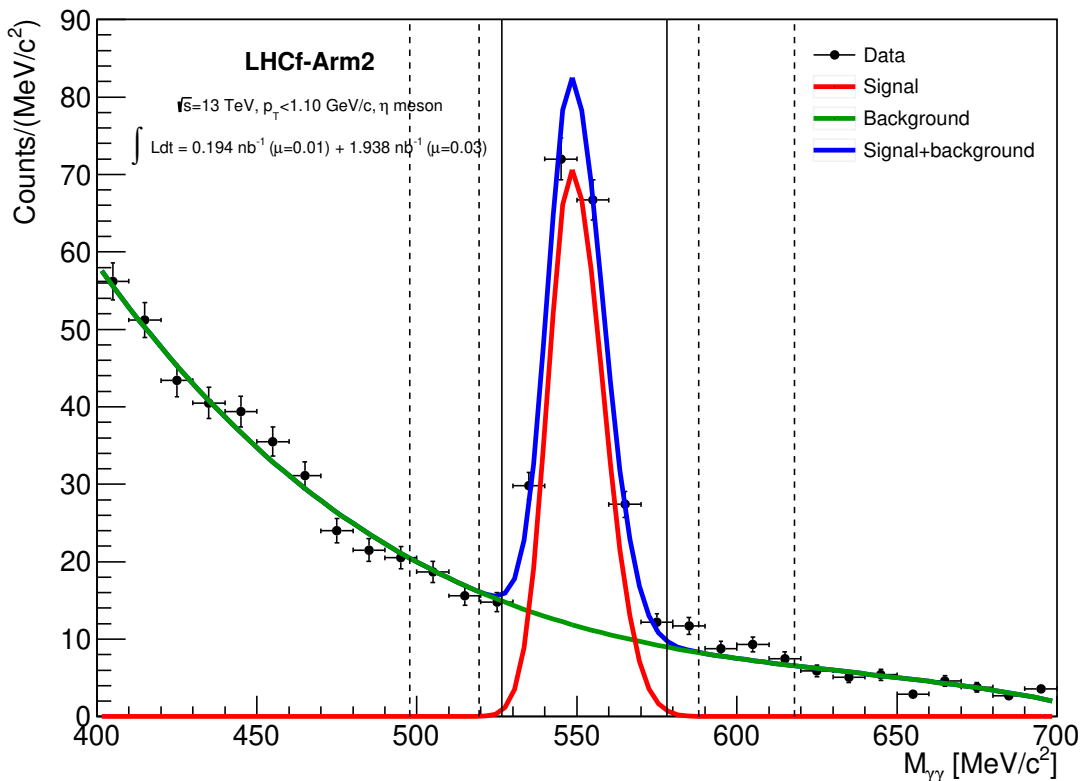


**Figure 3.** Di-photon invariant mass distribution reconstructed using the LHCf-Arm2 detector for pairs with  $p_T < 1.1$  GeV/c. The blue solid line shows the result of the composite fit on the distribution, obtained by adding the signal fit distribution (asymmetric Gaussian function, red line) and the background fit distribution (third-order Chebyshev polynomial function, green line). Solid and dashed vertical lines indicate the signal and the two background windows, respectively.

#### 4.2.2 Acceptance and branching ratio correction

Second, we corrected the signal distribution for the limited aperture of the LHCf-Arm2 detector since it does not cover the full  $2\pi$  azimuthal angle. To estimate the acceptance correction factors, we used a toy MC simulation based on the predictions from four hadronic interaction models, QGSJET II-04, EPOS-LHC, DPMJET 3.06 and SIBYLL 2.3. For each model, we generated an  $\eta$  meson  $p_t - x_F$  phase space, then we simulated the decay  $\eta \rightarrow \gamma\gamma$  and computed the  $p_t - x_F$  phase space for the particles hitting the LHCf-Arm2 detector, also considering the single-photon selection criteria on energy and position listed in table 2. The geometrical acceptance efficiency was calculated as the ratio of accepted  $\eta$  mesons divided by the distribution of all generated  $\eta$  mesons. The acceptance correction is defined as the inverse of the acceptance efficiency. The four models provide different predictions of the acceptance correction factor due to the different  $p_t - x_F$  spectrum shapes inside the  $x_F$  bins used in the analysis, as shown in figure 5, where both the acceptance maps (top panel) and the acceptance correction  $x_F$  distributions (bottom panel) of the models considered in the analysis are displayed. The final map applied to the data was obtained by averaging the results of the models in the analysis  $p_t - x_F$  region, defined by

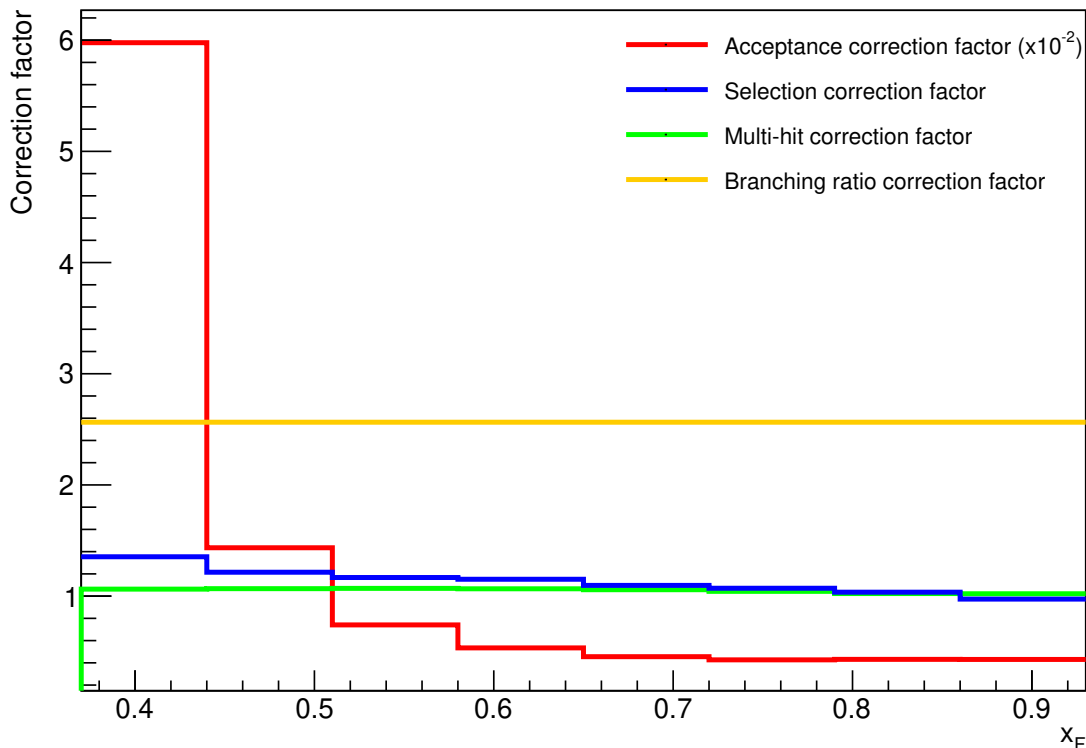


**Figure 4.** Corrections for experimental effects in the LHCf-Arm2 detector, applied to the final  $x_F$  spectrum. The acceptance correction is scaled for a factor  $10^{-2}$ . Statistical uncertainties on the curves are negligible, thanks to the high statistics of the generated Monte Carlo datasets for each hadronic interaction model (see table 1). Systematic errors related to the model-dependence of the corrections are discussed in section 4.3.6.

$p_T < 1.1 \text{ GeV}/c$  and  $0.37 \leq x_F \leq 0.93$  and by calculating the acceptance correction using the same binning of the experimental distribution, as shown in bottom panel of figure 5. The analysis region is indicated by red boxes in the acceptance maps shown in the top panel of figure 5. A systematic uncertainty was calculated using the method described in section 4.3.6 to account for the differences between these models. The branching ratio of the  $\eta$  decay into two photons is  $(39.41 \pm 0.18)\%$ . We also corrected for this inefficiency by applying a constant factor to the signal distribution in the whole  $x_F$  range. Since the uncertainty of the branching ratio value of the two-photon decay of the  $\eta$  meson is less than 0.5%, we have neglected its contribution to the total uncertainty.

### 4.2.3 Multi-hit correction

Last, the inefficiency due to the multi-hit rejection was corrected. This inefficiency is due to the loss of  $\eta$  mesons when cutting the events with more than one particle per tower of the LHCf-Arm2 detector, described in section 4.1.1. The multi-hit correction factor is defined for each bin  $i$  of  $x_F$  as:

$$f_{\text{multi-hit}}^i = \frac{N_{\text{multi-hit}}^i + N_{\text{single-hit}}^i}{N_{\text{single-hit}}^i}. \quad (4.2)$$

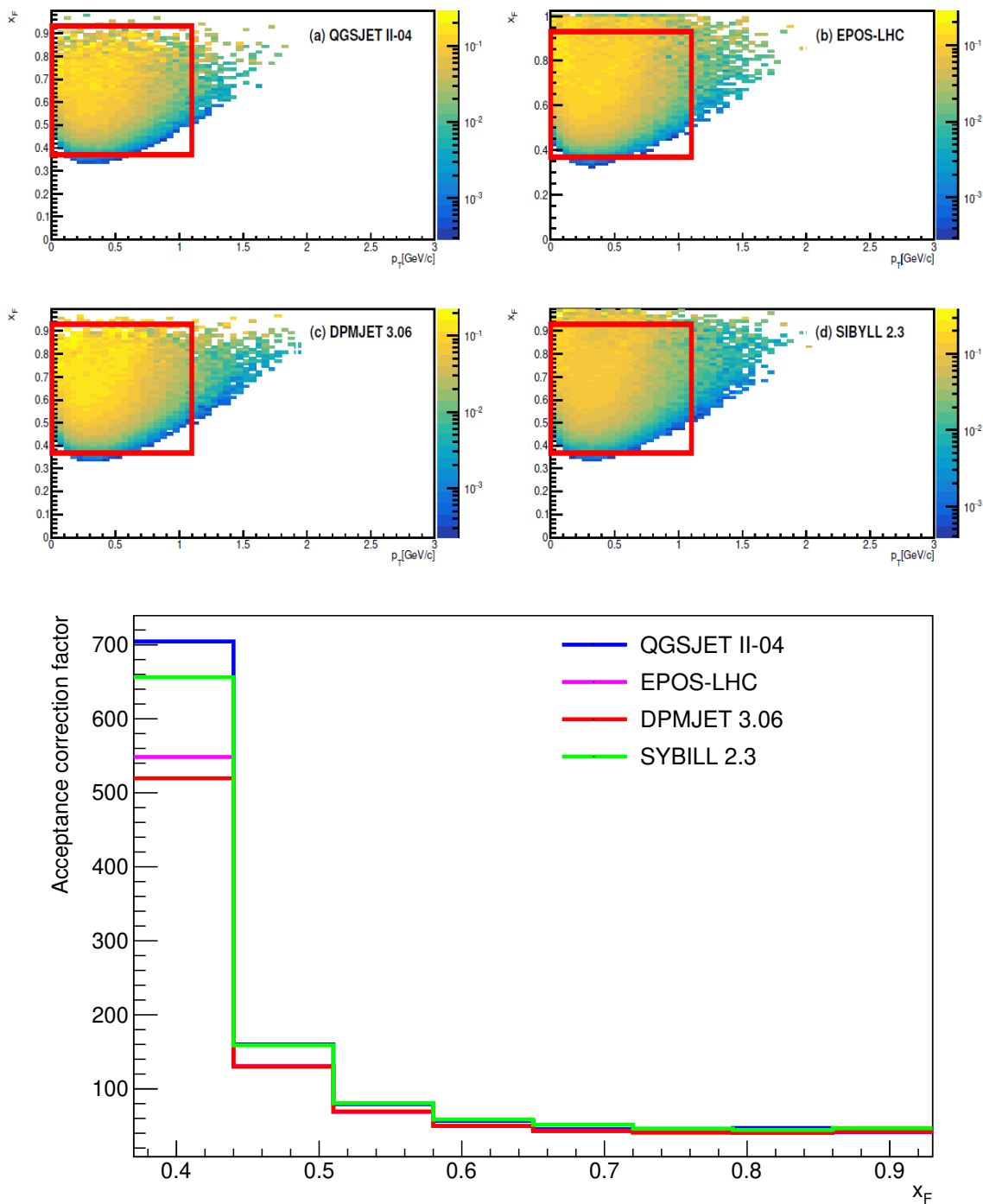


**Figure 5.** *Top:* acceptance maps of  $\eta$  detection by the LHCf-Arm2 detector in  $p_t - x_F$  phase space for the hadronic interaction models considered in the analysis. Position and energy threshold cuts are taken into account. The red boxes indicate the  $p_t - x_F$  analysis region of this analysis. *Bottom:* acceptance correction factor  $x_F$  distributions for different hadronic interaction models.

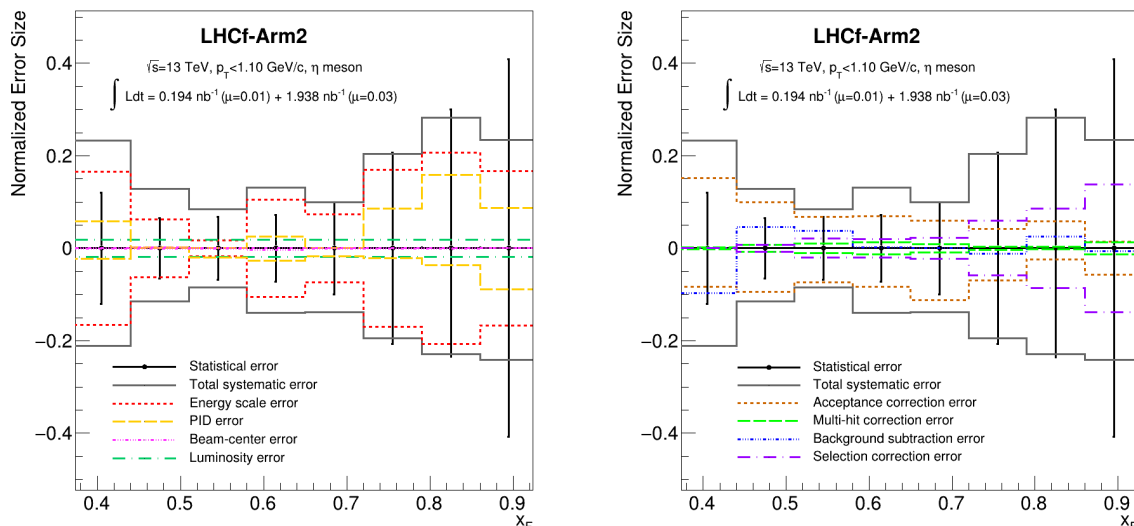


**Figure 6.** Relative systematical uncertainties of the  $\eta$  production cross section measured with the LHCf-Arm2 detector. Coloured lines refer to the single source of error while the grey line indicates the total systematic uncertainty, obtained by summing the contribution of each source in quadrature. Black markers indicate statistical errors. The left panel displays the systematics related to the operating conditions, while the right panel illustrates the systematics due to the use of Monte Carlo in the data analysis procedure.

where  $N_{\text{multi-hit}}^i$  is the number of multi-hit events while  $N_{\text{single-hit}}^i$  is the number of single-hit events, both for each bin  $i$  of  $x_F$ . Two corrections were calculated using the results of the full simulations of QGSJET II-04 and EPOS-LHC. To account for the differences between the two models, the signal distribution was corrected using the average of the correction factors obtained from them, and an additional systematic error was calculated according to the method reported in section 4.3.6.

### 4.3 Systematic uncertainties

The estimation of the total uncertainty on the  $x_F$  distribution of  $\eta$  is discussed in this section. A description of each source of error is given in sections 4.3.1–4.3.6. The total systematic error is calculated by quadratically summing the contribution of each source. Figure 6 shows the estimated systematic uncertainties as a function of  $x_F$ .

#### 4.3.1 Energy scale

As discussed in sections 4.1.4, systematic shifts in the invariant mass peaks of  $\pi^0$  and  $\eta$  were found with respect to the world averaged values of the rest mass of the two particles. The amount of the discrepancies were  $(-2.57 \pm 0.04)\%$  and  $(-2.65 \pm 0.20)\%$  for  $\pi^0$  and  $\eta$ , respectively. The two values were consistent within the errors and were also compatible with the uncertainty on the absolute energy scale, calculated using beam test data at SPS, and equal to  $\pm 2.7\%$  [37]. The two peaks were restored to the correct position by increasing the energies of individual photons by  $+2.65\%$ . In order to assess the uncertainty on the absolute energy scale, we decided to check the stability of this value as a function of the

energy. This was done for each tower by considering Type II events, which release all their energy in a single tower. Since Type II  $\eta$  are outside detector acceptance, we used Type II  $\pi^0$  for this purpose. In both towers, the stability of Type II  $\pi^0$  invariant mass throughout the energy range was within 1%, which was conservatively assumed as uncertainty on the absolute energy scale. The systematic errors on the energy scale were then obtained by producing two  $x_F$  distributions artificially scaling the single-photon energies by +1% and -1%, respectively, and taking the variation from the unscaled spectrum as the estimation of the systematic uncertainty. The upper and lower error bands were conservatively symmetrized by assigning to both the maximum of the two values for each bin of  $x_F$ .

### 4.3.2 PID

The systematic uncertainty associated with the particle identification method used in this analysis was calculated for every bin of the  $x_F$  distribution by comparing the spectra obtained with different PID criteria. Two additional  $L_{90\%}$  cut functions were calculated in the same way described in section 4.1.3 but using different values of the required efficiency, 85% and 95% instead of 90%. These limits were chosen to maintain the product of efficiency and purity above 75% in the full energy range. The whole analysis was then repeated with these different functions and the PID error was estimated using the relative deviation from the original distribution.

### 4.3.3 Beam-center stability

The beam-center was calculated by fitting the hit position of high-energy hadrons with a two-dimensional Gaussian function, since these particles are very collimated to the beam axis. The beam-center position was used in this work to define the analysis region, so the uncertainties on its determination affect the final distribution. To account for this effect, a systematic error was estimated by shifting the position of the beam-center of  $\pm 0.3$  mm in both the X and Y direction. This value is consistent with the parameter fluctuations observed run-by-run during the data taking. We compared the four obtained spectra with the original one and assigned the systematic uncertainties due to the beam-center stability as the relative deviations between them.

### 4.3.4 Luminosity

The uncertainty on the integrated luminosity measured by ATLAS was estimated to be  $\pm 1.9\%$ . This value was obtained using the methodology described in [24] for the LHC Fill 3855. Note that this is the only energy-independent systematic uncertainty.

### 4.3.5 Background subtraction

The uncertainty on the background subtraction method, explained in section 4.1.4, is evaluated using the full MC simulation based on QGSJET II-04. The whole analysis procedure is applied to this MC dataset, up to the step where the spectrum in  $x_F$  is extracted using the sideband method. Another  $x_F$  spectrum is generated rejecting background events using the MC truth information from the simulation. The relative variation between these two spectra is used to estimate the error associated to the background subtraction method.

### 4.3.6 MC related correction

As described in section 4.2.1–4.2.3, we used MC simulation to calculate several corrections, namely selection, acceptance and multi-hit corrections. A systematic error was calculated for each correction to avoid the model dependence on the final distribution. The selection and multi-hit corrections were calculated using the full reconstructed simulations based on QGSJET II-04 and EPOS-LHC. In this case, the errors were calculated by the relative deviation between the correction values predicted by the two models. For the acceptance correction, we used the prediction from four different models used in this analysis, QGSJET II-04, EPOS-LHC, DPMJET 3.06 and SIBYLL 2.3. The corresponding errors were calculated in the most conservative way by looking at the relative maximum and minimum differences between the model predictions of the correction value and the mean of the values.

## 5 Results

The  $x_F$  spectrum of  $\eta$  mesons measured by the LHCf-Arm2 detector in  $p_T < 1.1$  GeV/c is presented in figure 7. The inclusive production rate is given by the expression:

$$\frac{1}{\sigma_{\text{inel}}} x_F \frac{d\sigma}{dx_F}. \quad (5.1)$$

$\sigma_{\text{inel}}$  is the inelastic cross section for proton-proton collisions at  $\sqrt{s} = 13$  TeV, measured by the TOTEM experiment [38] as  $\sigma_{\text{inel}} = (79.5 \pm 1.8)$  mb [39]. Even considering the measurement of the inelastic cross section made by other LHC experiments [40, 41], the difference is minimal and the resulting uncertainty on  $\eta$  production rate is negligible. The quantity  $x_F d\sigma/dx_F$  is the differential cross section of  $\eta$  production, with  $d\sigma = dN_\eta / \int L dt$ , where  $dN_\eta$  is the number of  $\eta$  mesons and  $\int L dt$  the integrated luminosity of the dataset. The black error bars in figure 7 represent the statistical uncertainties, while the grey shaded areas are the total uncertainties obtained by summing statistical and systematic errors in quadrature. The inclusive  $\eta$  production rate values for each bin of  $x_F$  and the total uncertainties are shown in table 3. In figure 7 the prediction of several hadronic interaction models at the generator level, QGSJET II-04, EPOS-LHC, DPMJET 3.06 and SIBYLL 2.3, and their ratio to experimental data are also reported. QGSJET II-04 shows the best agreement with LHCf data among the models tested in this analysis, especially for  $x_F > 0.7$ , but about a factor 2 of difference is found at lower  $x_F$ . The other three models, EPOS-LHC, DPMJET 3.06 and SIBYLL 2.3 predict higher production rates and a harder spectrum with respect to experimental data in the whole  $x_F$  range. The values of the ratios for each model and for each  $x_F$  bin are reported in table 4.

## 6 Conclusions

The LHCf experiment measured the inclusive production rate of  $\eta$  mesons in proton-proton collisions at  $\sqrt{s} = 13$  TeV in  $p_T < 1.1$  GeV/c. About 1500 candidate  $\eta$  mesons were found in the dataset considered for this analysis; this is both the first measurement of  $\eta$  mesons from LHCf and the first time a particle containing strange quarks has been observed in the very

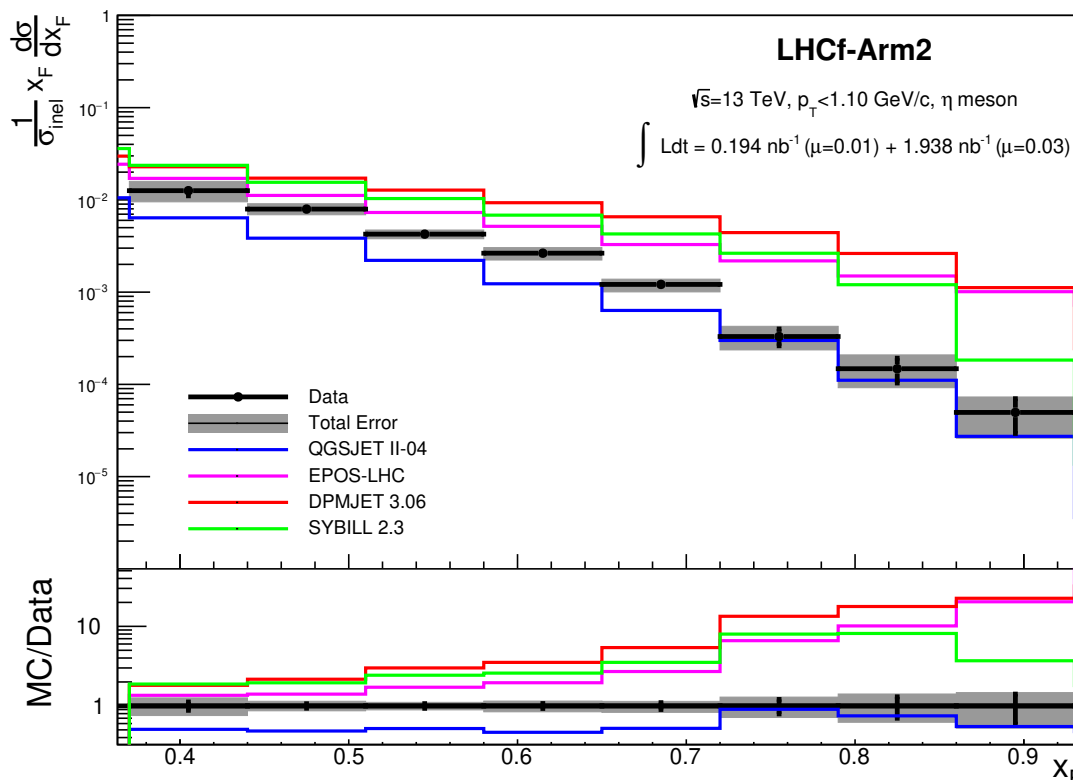


**Figure 7.** Inclusive  $\eta$  production rate as function of  $x_F$  in  $p_T < 1.1$  GeV/c for p-p collisions at  $\sqrt{s} = 13$  TeV, measured using the LHCf-Arm2 detector. Black markers refer to experimental data with statistical errors and grey bands refer to the total uncertainties, obtained by summing in quadrature the statistical and systematic errors. The data points are compared with the prediction, at the generator level, of the hadronic interaction models considered in this analysis, QGSJET II-04 (blue line), EPOS-LHC (magenta line), SIBYLL 2.3 (green line) and DPMJET 3.06 (red line).

forward region for high-energy collisions. The result was compared with the prediction of several hadronic interaction models, QGSJET II-04, EPOS-LHC, DPMJET 3.06 and SIBYLL 2.3. None of the models reproduces the experimental distribution in the whole  $x_F$  range. QGSJET II-04 shows the best agreement, but significant differences are present at low  $x_F$ . The other models predict an overall higher production rate than the experimental data. The large experimental uncertainties in this analysis, due to the low accumulated statistics, will be improved by the new LHCf data collected during LHC RUN III, in which an increase in eta meson statistics by about a factor of ten is expected [18].

## Acknowledgments

We thank the CERN staff and the ATLAS collaboration for their essential contributions to the successful operation of LHCf. We are grateful to S. Ostapchenko for useful comments about QGSJET II-04 generator and to the developers of CRMC interface tool for its implementation. This work was supported by several institutions in Japan and in Italy: in Japan, by the Japanese Society for the Promotion of Science (JSPS) KAKENHI

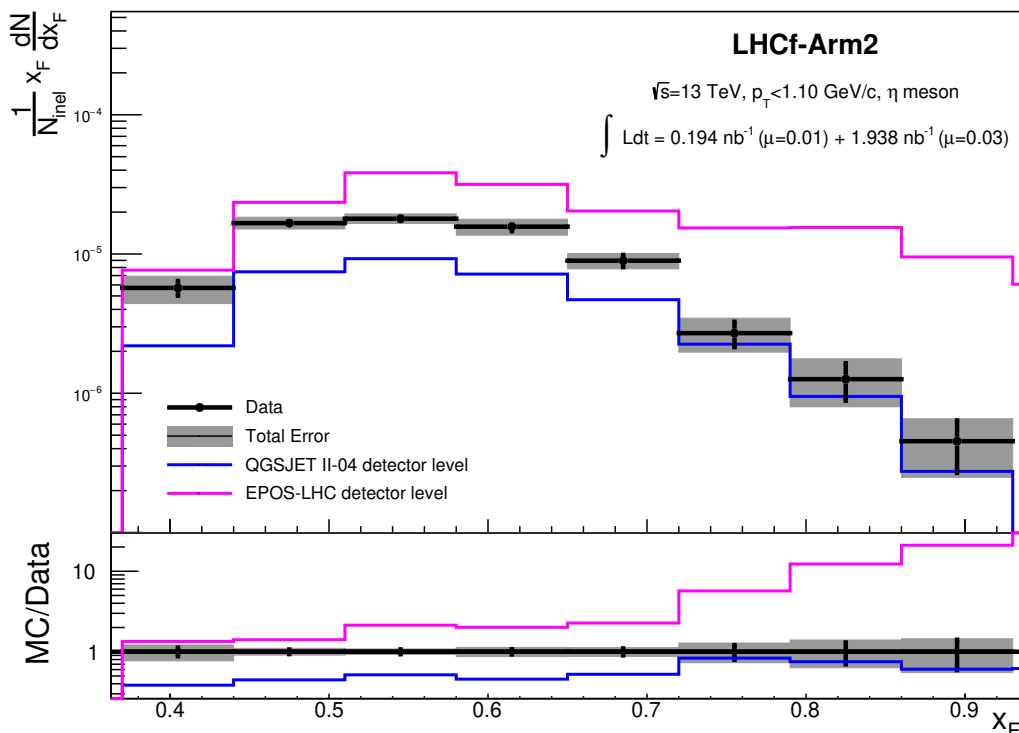


**Figure 8.** Detector level comparison between measured production (black markers) rate and the prediction of the Monte Carlo simulation based on the QGSJET II-04 (blue line) and EPOS-LHC models (magenta line). The results refer to proton-proton collisions at  $\sqrt{s} = 13$  TeV, in  $p_T < 1.1$  GeV/c. The total error (grey bands) is calculated considering only systematic uncertainties based on the operating conditions (see left panel of figure 6).

(Grant Numbers JP26247037, JP23340076) and the joint research program of the Institute for Cosmic Ray Research (ICRR), University of Tokyo; in Italy, by Istituto Nazionale di Fisica Nucleare (INFN) and by the University of Catania (Grant Numbers UNICT 2020-22 Linea 2). This work took advantage of computer resources supplied by ICRR (University of Tokyo), CERN and CNAF (INFN).

## A Production rate distributions at the detector level

To perform corrections on the experimental distribution we used fully reconstructed MC simulations based on the QGSJET II-04 and the EPOS-LHC models, as described in section 4.2. To avoid model-dependent bias we tested the agreement of the detector level distributions of experimental data and MC simulations. The comparison is presented in figure 8. The use of the simulations based on the two models to make the corrections is justified by the similar level of agreement between the data and MC before and after the corrections. Furthermore, the fact that the measured values are approximately in the middle between the predictions of the two models justifies using the average of the corrections obtained between the two simulations as the final correction factor.

## B Cross section tables

Inclusive  $\eta$  production rate values as function of  $x_F$  in  $p_T < 1.1$  GeV/c measured by LHCf-Arm2 in p-p collisions at  $\sqrt{s} = 13$  TeV are summarized in table 3. The ratios of the  $\eta$  production rate of hadronic interaction models to data are summarized in table 4.

$x_F$ range	$(x_F/\sigma_{\text{inel}})(d\sigma/dx_F)$
[0.37–0.44]	$(1.26_{-0.31}^{+0.33}) \times 10^{-2}$
[0.44–0.51]	$(0.79_{-0.11}^{+0.11}) \times 10^{-2}$
[0.51–0.58]	$(4.25_{-0.46}^{+0.46}) \times 10^{-3}$
[0.58–0.65]	$(2.64_{-0.42}^{+0.40}) \times 10^{-3}$
[0.65–0.72]	$(1.21_{-0.21}^{+0.17}) \times 10^{-3}$
[0.72–0.79]	$(3.30_{-0.94}^{+0.96}) \times 10^{-4}$
[0.79–0.86]	$(1.48_{-0.56}^{+0.61}) \times 10^{-4}$
[0.86–0.93]	$(0.50_{-0.24}^{+0.23}) \times 10^{-4}$

**Table 3.** Inclusive  $\eta$  production rate for each bin of  $x_F$  in  $p_T < 1.1$  GeV/c, measured using the LHCf-Arm2 in p-p collisions at  $\sqrt{s} = 13$  TeV. Total uncertainties are also reported.

$x_F$ range	QGSJET	EPOS	SIBYLL	DPMJET
	II-04	LHC	2.3	3.06
[0.37–0.44]	0.51	1.36	1.88	1.81
[0.44–0.51]	0.48	1.41	1.95	2.16
[0.51–0.58]	0.52	1.72	2.43	3.00
[0.58–0.65]	0.47	1.95	2.58	3.52
[0.65–0.72]	0.52	2.70	3.53	5.41
[0.72–0.79]	0.91	6.61	7.99	13.38
[0.79–0.86]	0.75	10.12	8.14	17.76
[0.86–0.93]	0.55	20.36	3.69	22.54

**Table 4.** Ratio of inclusive  $\eta$  production rates of hadronic interaction models to data in p-p collision at  $\sqrt{s} = 13$  TeV for each  $x_F$  bin in  $p_T < 1.1$  GeV/c.

**Open Access.** This article is distributed under the terms of the Creative Commons Attribution License ([CC-BY 4.0](https://creativecommons.org/licenses/by/4.0/)), which permits any use, distribution and reproduction in any medium, provided the original author(s) and source are credited.

## References

- [1] PIERRE AUGER collaboration, *Observation of the suppression of the flux of cosmic rays above  $4 \times 10^{19}$  eV*, *Phys. Rev. Lett.* **101** (2008) 061101 [[arXiv:0806.4302](#)] [[INSPIRE](#)].
- [2] PIERRE AUGER collaboration, *Update on the Correlation of the Highest Energy Cosmic Rays with Nearby Extragalactic matter*, *Astropart. Phys.* **34** (2010) 314 [[arXiv:1009.1855](#)] [[INSPIRE](#)].
- [3] PIERRE AUGER collaboration, *Measurement of the Depth of Maximum of Extensive Air Showers above  $10^{18}$  eV*, *Phys. Rev. Lett.* **104** (2010) 091101 [[arXiv:1002.0699](#)] [[INSPIRE](#)].
- [4] R.U. Abbasi et al., *Measurement of the Flux of Ultra High Energy Cosmic Rays by the Stereo Technique*, *Astropart. Phys.* **32** (2009) 53 [[arXiv:0904.4500](#)] [[INSPIRE](#)].
- [5] R.U. Abbasi et al., *Analysis of Large-Scale Anisotropy of Ultra-High Energy Cosmic Rays in HiRes Stereo Data*, *Astrophys. J. Lett.* **713** (2010) L64 [[arXiv:1002.1444](#)] [[INSPIRE](#)].
- [6] HIGH RESOLUTION FLY'S EYE collaboration, *Indications of Proton-Dominated Cosmic Ray Composition above 1.6 EeV*, *Phys. Rev. Lett.* **104** (2010) 161101 [[arXiv:0910.4184](#)] [[INSPIRE](#)].
- [7] TELESCOPE ARRAY collaboration, *Recent results from the Telescope Array experiment*, *AIP Conf. Proc.* **1367** (2011) 17.
- [8] PIERRE AUGER collaboration, *The Pierre Auger Cosmic Ray Observatory*, *Nucl. Instrum. Meth. A* **798** (2015) 172 [[arXiv:1502.01323](#)] [[INSPIRE](#)].
- [9] M. Fukushima, *Telescope array project for extremely high energy cosmic rays*, *Prog. Theor. Phys. Suppl.* **151** (2003) 206 [[INSPIRE](#)].
- [10] PIERRE AUGER collaboration, *Depth of Maximum of Air-Shower Profiles at the Pierre Auger Observatory: Measurements at Energies above  $10^{17.8}$  eV*, *Phys. Rev. D* **90** (2014) 122005 [[arXiv:1409.4809](#)] [[INSPIRE](#)].
- [11] PIERRE AUGER collaboration, *Muons in Air Showers at the Pierre Auger Observatory: Measurement of Atmospheric Production Depth*, *Phys. Rev. D* **90** (2014) 012012 [*Addendum ibid.* **90** (2014) 039904] [[arXiv:1407.5919](#)] [[INSPIRE](#)].
- [12] R.U. Abbasi et al., *Study of Ultra-High Energy Cosmic Ray composition using Telescope Array's Middle Drum detector and surface array in hybrid mode*, *Astropart. Phys.* **64** (2015) 49 [[arXiv:1408.1726](#)] [[INSPIRE](#)].
- [13] V.N. Gribov, *A reggeon diagram technique*, *Sov. Phys. JETP* **26** (1968) 414 [*Zh. Eksp. Teor. Fiz.* **53** (1967) 654] [[INSPIRE](#)].
- [14] T. Regge, *Introduction to complex orbital momenta*, *Nuovo Cim.* **14** (1959) 951 [[INSPIRE](#)].
- [15] L. Evans and P. Bryant, *LHC Machine*, *2008 JINST* **3** S08001 [[INSPIRE](#)].
- [16] J. Albrecht et al., *The Muon Puzzle in cosmic-ray induced air showers and its connection to the Large Hadron Collider*, *Astrophys. Space Sci.* **367** (2022) 1.
- [17] LHCf collaboration, *The LHCf detector at the CERN Large Hadron Collider*, *2008 JINST* **3** S08006 [[INSPIRE](#)].
- [18] O. Adriani et al., *LHCf — Technical Proposal for the LHC Run3*, *CERN-LHCC-2019-008* (2019).

- [19] T. Suzuki et al., *Performance of very thin Gd<sub>2</sub>SiO<sub>5</sub> scintillator bars for the LHCf experiment*, [2013 JINST 8 T01007](#) [INSPIRE].
- [20] O. Adriani et al., *The construction and testing of the silicon position sensitive modules for the LHCf experiment at CERN*, [2010 JINST 5 P01012](#) [INSPIRE].
- [21] Y. Makino et al., *Performance study for the photon measurements of the upgraded LHCf calorimeters with Gd<sub>2</sub>SiO<sub>5</sub> (GSO) scintillators*, [2017 JINST 12 P03023](#) [INSPIRE].
- [22] K. Kawade et al., *The performance of the LHCf detector for hadronic showers*, [2014 JINST 9 P03016](#) [[arXiv:1312.5950](#)] [INSPIRE].
- [23] LHCf collaboration, *LHCf experiment: Technical Design Report*, CERN-LHCC-2006-004 (2006).
- [24] ATLAS collaboration, *Luminosity determination in pp collisions at  $\sqrt{s} = 13$  TeV using the ATLAS detector at the LHC*, [arXiv:2212.09379](#) [INSPIRE].
- [25] K. Kasahara, *Cosmos*, (2010) <http://cosmos.n.kanagawa-u.ac.jp/cosmosHome/index.html>.
- [26] K. Kasahara, *EPICS*, (2010) <http://cosmos.n.kanagawa-u.ac.jp/EPICSHome/index.html>.
- [27] S. Ostapchenko, *Monte Carlo treatment of hadronic interactions in enhanced Pomeron scheme. Part I. QGSJET-II model*, *Phys. Rev. D* **83** (2011) 014018 [[arXiv:1010.1869](#)] [INSPIRE].
- [28] T. Pierog, I. Karpenko, J.M. Katzy, E. Yatsenko and K. Werner, *EPOS LHC: Test of collective hadronization with data measured at the CERN Large Hadron Collider*, *Phys. Rev. C* **92** (2015) 034906 [[arXiv:1306.0121](#)] [INSPIRE].
- [29] F.W. Bopp, J. Ranft, R. Engel and S. Roesler, *Antiparticle to Particle Production Ratios in Hadron-Hadron and d-Au Collisions in the DPMJET-III Monte Carlo*, *Phys. Rev. C* **77** (2008) 014904 [[hep-ph/0505035](#)] [INSPIRE].
- [30] R. Ulrich, T. Pierog and C. Baus, *Cosmic Ray Monte Carlo Package, CRMC*, [[DOI:10.5281/ZENODO.5270381](#)].
- [31] F. Riehn, R. Engel, A. Fedynitch, T.K. Gaisser and T. Stanev, *A new version of the event generator Sibyll*, *PoS ICRC2015* (2016) 558 [[arXiv:1510.00568](#)] [INSPIRE].
- [32] LHCf collaboration, *Measurement of forward neutral pion transverse momentum spectra for  $\sqrt{s} = 7$  TeV proton-proton collisions at LHC*, *Phys. Rev. D* **86** (2012) 092001 [[arXiv:1205.4578](#)] [INSPIRE].
- [33] R.L. Workman et al., *Review of particle physics*, *Prog. Theor. Exp. Phys.* **2022** (2022) 083C01.
- [34] LHCf collaboration, *Measurements of longitudinal and transverse momentum distributions for neutral pions in the forward-rapidity region with the LHCf detector*, *Phys. Rev. D* **94** (2016) 032007 [[arXiv:1507.08764](#)] [INSPIRE].
- [35] M. Morháč, J. Kliman, V. Matoušek, M. Veselský and I. Turzo, *Background elimination methods for multidimensional coincidence gamma-ray spectra*, *Nucl. Instrum. Meth. A* **401** (1997) 113 [INSPIRE].
- [36] R. Brun and F. Rademakers, *ROOT: An object oriented data analysis framework*, *Nucl. Instrum. Meth. A* **389** (1997) 81 [INSPIRE].

- [37] LHCf collaboration, *Measurement of forward photon production cross-section in proton-proton collisions at  $\sqrt{s} = 13$  TeV with the LHCf detector*, *Phys. Lett. B* **780** (2018) 233 [[arXiv:1703.07678](#)] [[INSPIRE](#)].
- [38] TOTEM collaboration, *The TOTEM experiment at the CERN Large Hadron Collider*, *2008 JINST* **3** S08007 [[INSPIRE](#)].
- [39] G. Antchev et al., *First measurement of elastic, inelastic and total cross-section at  $\sqrt{s} = 13$  TeV by TOTEM and overview of cross-section data at LHC energies*, *Eur. Phys. J. C* **79** (2019) 1.
- [40] ATLAS collaboration, *Measurement of the Inelastic Proton-Proton Cross Section at  $\sqrt{s} = 13$  TeV with the ATLAS Detector at the LHC*, *Phys. Rev. Lett.* **117** (2016) 182002 [[arXiv:1606.02625](#)] [[INSPIRE](#)].
- [41] LHCb collaboration, *Measurement of the inelastic pp cross-section at a centre-of-mass energy of 13 TeV*, *JHEP* **06** (2018) 100 [[arXiv:1803.10974](#)] [[INSPIRE](#)].